Mon. Not. R. Astron. Soc. **000**, 000–000 (0000) Printed 4 April 2018

Probing the dynamics of cluster-lenses

Priyamvada Natarajan & Jean-Paul Kneib⋆
Institute of Astronomy, Madingley Road, Cambridge CB3 0HA

4 April 2018

ABSTRACT
We propose a new approach to study the dynamical implications of mass models of clusters for the velocity structure of galaxies in the core. Strong and weak lensing data are used to construct the total mass profile of the cluster, which is used in conjunction with the optical galaxy data to solve in detail for the nature of galaxy orbits and the velocity anisotropy in the central regions. We also examine other observationally and physically motivated mass models, specifically those obtained from X-ray observations and N-body simulations. The aim of this analysis is to understand qualitatively the structure of the core and test some of the key assumptions of the standard picture of cluster formation regarding relaxation, virialization and equilibrium. This technique is applied to the cluster Abell 2218, where we find evidence for an anisotropic core, which we interpret to indicate the existence of a dynamically disturbed central region. We find that the requirement of physically meaningful solutions for the velocity anisotropy places stringent bounds on the slope of cluster density profiles in the inner regions.

Key words: galaxy clusters: lensing – galaxy clusters: galaxy orbits – galaxy clusters: dynamics

1 INTRODUCTION

Studying the velocity structure of the cores of clusters of galaxies promises to provide new insights into the physics of the formation of clusters. The crucial physical consequence of the cumulative dynamical history of a cluster is its underlying mass distribution. We propose a new approach to study the dynamics of cluster galaxies using the mass profile measured from gravitational lensing. Lensing provides the most accurate determination of the mass profile, and is independent of assumptions as to the kinematics of the cluster.

The dramatic arcs and multiple images produced by rich clusters tightly constrains the mass of the cluster in the inner-most regions, on the scale of the Einstein radius, with typical range $30 < r_E < 200\,h_{50}^{-1}$ kpc (Kneib & Soucail 1996). Current progress in observational techniques have made it possible to map the cluster mass out to large radii from the weak shearing of faint background galaxies. While uncertainties arise due to the correction for the point-spread function and the unknown redshift-distribution of background galaxies, reliable mass profiles for an increasing number of clusters should be available in the near future (Kaiser, Squires, & Broadhurst 1995). Combining this with knowledge of the spatial distribution and line-of-sight component of the velocities of cluster galaxies, and assuming them to be good tracers of the cluster potential well, we can solve in detail for the variation of the velocity anisotropy parameter β with distance from the cluster centre.

It is an observational challenge to perform a comprehensive redshift survey of distant clusters, $z > 0.1$ in sufficient detail to interpret the velocity histogram and efficiently disentangle the effects of substructure, existence of velocity anisotropy and axisymmetric infall. However, securing 200 to 800 velocities for distant cluster galaxies is now becoming possible with the newly developed MOS multi-object imaging spectrographs (Yee, Ellingson, & Carlberg (1996a) and Lefevre et al. (1994)). This would enable constructing secure line-of-sight velocity dispersion profiles for high redshift clusters.

Recent optical surveys by Colless & Dunn (1996) and X-ray studies of clusters by Briel & Henry (1995) seem to indicate that while the X-ray isophotes of cluster cores have an overall smooth appearance most of them are not only dynamically young but also quite disturbed. The nature of orbits is therefore an important indicator of the dynamical state of both the inner and outer regions of the cluster. Principally radial orbits, expected at the outskirts, are the signature of a region dominated by infall, whereas isotropic orbits imply the existence of a well-mixed region.

Previous studies of the velocity dispersion profile and estimates of the degree of anisotropy in clusters have provided ambiguous results, primarily due to the lack of knowl-

⋆ Present address: Observatoire Midi-Pyrenees, 14 Av. E.Belin, 31400 Toulouse, France

edge of the underlying mass distribution. The velocity structure of galaxies in clusters have been studied in detail (Coma and A2670) by Kent & Gunn (1982); The & White (1986); Merritt (1987); Sharples, Ellis, & Gray (1988); Colless & Dunn (1996) and several other groups. These analyses used the observed galaxy positions and velocities to constrain the distribution of total mass and simultaneously find consistent and physically meaningful solutions for the velocity anisotropy.

The & White (1986) examined the uncertainties in the virial mass profiles derived for Coma from observational data. They showed that a wide range of mass models are consistent, consequently permitting a large range of orbital structures. Mass models that were more compact (but had low overall masses) implied circular orbits for the galaxies whereas the higher mass models implied predominantly radial orbits. Merritt (1987) examined the relative distribution of the dark and luminous matter in Coma and showed that it was impossible to distinguish between models where the galaxies trace the total mass and were on isotropic orbits versus those in which the dark matter was very concentrated and the galaxies were on primarily transverse orbits. Therefore, sufficient constraints on the total mass distribution and the velocity anisotropy cannot be obtained simultaneously using only the luminous tracers. In the recent survey of the Coma cluster by Colless & Dunn (1996), they find that the velocity distribution is highly non-Gaussian. The dynamics can be better interpreted in terms of an on-going merger between two sub-clusters, thus indicating that the system is not in virial equilibrium.

Similar studies of the cluster A2670 have also been inconclusive; in the faint photometric and spectroscopic survey by Sharples, Ellis, & Gray (1988), both extremely anisotropic models and nearly isotropic ones were indistinguishable in terms of goodness of fit with respect to the available data.

In these clusters and others that have been studied, the principal uncertainty in the determination of the anisotropy arises from ignorance of the distribution of the total mass. In our analysis, independent data from lensing that constrains the overall mass distribution allows the elimination of this largest source of uncertainty.

The plan of this paper is as follows: in Section 2 we review observational probes of the internal dynamics of clusters and construct mass models from X-ray data, lensing data, and from N-body simulations. The mathematical formalism that forms the basis of our approach is presented in Sections 3 & 4. The robustness of the method is demonstrated for several fiducial forms of the total mass profile (Section 5), and the technique is then applied to the cluster A2218 (Section 6). Finally, we discuss our results and their implications for the physical state of the core of A2218. Throughout this paper, we assume $H_0 = 50\,\mathrm{km\ s^{-1}Mpc^{-1}}$, $\Omega = 1$ and $\Lambda = 0$.

2 OBSERVED PROPERTIES OF THE CORE

2.1 Photometric and spectroscopic studies

With the rapid progress in photometric and spectroscopic techniques, the precision of observationally determined parameters for clusters has improved significantly in the past decade. The main limitations are the errors incurred in establishing cluster membership (Aragon-Salamanca et al. 1993) due to contamination from the field population for photometrically selected samples. On the spectroscopic front, while surveys are pushing down to fainter magnitude limits, a commensurate gain in the number of cluster galaxies sampled cannot be achieved since the number of faint background field galaxies grows more rapidly. In the following subsections we examine the observationally determined quantities that we use in our present analysis.

2.1.1 Galaxy surface density profiles from optical data

Galaxy surface density profiles are generally determined by fitting the observed number density in a given cluster to physically motivated functional forms (Kent & Gunn 1982). Since to define cluster membership, one usually uses the color-magnitude relation of the E & S0 galaxies (given the limited spectroscopic samples available), the computed galaxy distribution profile preferentially probes the E & S0 cluster galaxies. The other morphological types in the cluster, could in principle have different profiles, but given the limitations of the available data we implicitly assume that the E & S0's efficiently trace the overall mass distribution.

While it can be argued that there is insufficient observational evidence for a core in the galaxy distribution in clusters (Carlberg et al. (1996) and Merritt & Tremblay (1994)), it is nevertheless instructive to examine the modified Hubble law profile which provides a reasonable fit to sparser samples.
PROFILE A:

$$\nu_g(r) = \frac{\nu_0}{(1 + \frac{r^2}{r_g^2})^{1.5}}. \tag{1}$$

The core radius r_g for typical clusters ranges from $150\,h_{50}^{-1}$ kpc to about $300 h_{50}^{-1}$ kpc. A least squares method is then used to determine the values of ρ_0 and core radius that simultaneously provide the best-fit to the data. For well-sampled clusters, (Katgert et al. (1996) and Yee, Ellingson, & Carlberg (1996b)) it is found that the number density of galaxies can be fit by a generic profile of the form,
PROFILE B:

$$\nu_g(r) = \frac{\nu_0}{(\frac{r}{s})^{\alpha}(1 + \frac{r}{s})^{2-\alpha}}, \tag{2}$$

with $\alpha = 1$ and s being a scale-radius ranging from $200 - 400 h_{50}^{-1}$ kpc. This profile looks asymptotically like the modified Hubble law, but has a central cusp. We examine both these profiles and their implications for the core dynamics in detail in Section 5 of this paper.

In principle, non-parametric maximum-likelihood and regression techniques developed by Merritt & Gebhardt (1995) and Merritt & Tremblay (1994) are more accurate in terms of characterizing the surface number density distribution; given the quality of data available at present for lensing clusters (at moderately high redshift) with a secure mass model, good photometry and sufficient velocities, we restrict our current analysis to a parametric approach, primarily on the basis of statistical adequacy given the sample

sizes that we are dealing with and the convenience of working with analytic forms. Besides, the non-parametric methods necessarily involve smoothing the data in order to yield confidence limits, which introduces a bias that increases with the degree of smoothing employed and is hence undesirable for sparse samples. For a more complete data-set however, a non-parametric likelihood method would be more appropriate.

2.1.2 Line-of-sight velocity dispersion profiles

The only measured component of the velocity dispersion of the galaxies is the projection along the line-of-sight. The interpretation of this measurement might be severely affected by substructure in the cluster and the presence of interacting sub-groups. For any distant cluster ($z > 0.1$), the line-of-sight velocity dispersion is not determined accurately enough at present to construct a secure radial profile. Even for nearby clusters, the rich region close to the centre and the outer regions, are not sampled adequately to infer conclusively the asymptotic behavior. For the well-studied cluster Abell 2218, the error bars in the measurements (see Fig. 6) are too large to perform any sensible fit to the available data and extract a radial profile.

2.1.3 X-ray observations

X-ray observations by Einstein, ROSAT and ASCA map the thermal bremsstrahlung emission from the hot intracluster gas at temperatures around $10^7 - 10^8 K$; the typical observed X-ray luminosities range from $10^{42} - 10^{45}$ ergs s^{-1} (in the $0.5 - 4.5$ keV band). The measured gas mass within the central few Mpc is of the order of $10^{14}\, M_\odot$, and the inferred cooling times for the gas in some clusters is of the order of 10^9 years (Fabian, Nulsen, & Canizares 1982). The surface brightness profiles of clusters are sharply peaked at the centre. From X-ray observations, with a few exceptions, most cluster cores appear smooth and uniform with very regular isophotes. Accurate measurements of the temperature profile in the cores are only now becoming feasible (for $z < 0.1$ clusters) with the ASCA satellite.

2.1.4 Mass profiles from X-ray data

Standard deprojection analysis of the X-ray surface brightness profile gives the density profile of the gas, and the cluster potential within which the gas is confined (Sarazin 1988). The main limiting assumptions are spherical symmetry, hydrostatic equilibrium, the inability to take sub-structure into account and assumptions regarding the unknown radial temperature profile of the gas (Nulsen & Böhringer 1995). The latter assumption is particularly important when modelling the inner parts of cluster cores with either strong cooling flows, where one expects to have a multiphase ICM (Allen, Fabian, & Kneib 1996), or in clusters which have undergone recent mergers, resulting in a complex temperature structure. Preliminary results of measurements of the temperature structure of the core of A2256 (Briel & Henry 1995) seem to indicate that this cluster, which was believed to be one of the smoothest and most uniform from its X-ray image shows strong evidence for temperature gradients in the core (Markevitch et al. 1996).

2.2 N-body simulations

N-body simulations provide the crucial link in understanding how the observed structure in clusters arises in the context of their evolution from the initial perturbations in the gravitational instability picture.

High-resolution simulations that incorporate gas dynamics and some of the important gas physics like shocks and radiative cooling are being used to study the formation, dynamics and evolution of galaxy clusters in the scenario where structure is built up hierarchically in a universe dominated by cold dark matter (Evrard 1990;Cen, Gnedin, & Ostriker 1993; Navarro & White 1994; Frenk et al. 1995). The evolution of both the dark matter and the baryonic component can be tracked to within the resolution limit. While the core of an individual cluster cannot be resolved in enough detail to understand relaxation processes, an ensemble of clusters can be studied for their 'average' properties (Navarro, Frenk, & White 1994).

The density profiles of clusters formed in these simulations are sensitive to the underlying cosmological model, the initial conditions, the accuracy of modelling gas dynamic processes and prescriptions for galaxy and star formation. Efsthathiou et al. (1985) found that in simulations with only dark matter particles, the slope of the density profile on cluster scales steepens with increasing n, where n is the spectral index of the scale-free, initial perturbations in an Einstein-de Sitter cosmology. It has been suggested by Crone, Evrard, & Richstone (1994) and Navarro, Frenk, & White (1994) that ensemble cluster properties, like abundance, clustering and density profiles might be a useful discriminant of cosmological parameters. However, properties of currently simulated clusters are not consistent in detail with their observed properties, primarily a reflection of the lack of understanding of the physics of galaxy formation and the role of non-gravitational processes coupled with the lack of knowledge of Ω. Qualitatively though, the morphology of simulated clusters is quite similar to ROSAT observations of X-ray clusters, and the physical effects of mass segregation due to dynamical friction and luminosity segregation seem to be borne out in the simulations - evidence to support our naive theoretical picture of the formation of clusters.

In a recent paper, Navarro, Frenk, & White (1996) report the results of their N-body + SPH simulations, wherein a 'universal density profile' is found to be a good fit over a large range of scales for dark halos in standard CDM models. The halo profiles are more or less isothermal, shallower than r^{-2} near the central regions and steeper close to the virial radius. The density profile has the following form,

$$\rho\,(r) = \frac{\rho_0}{\frac{r}{r_s}(1+\frac{r}{r_s})^2} \tag{3}$$

where r_s is a scale radius. The corresponding mass profile is given by:

$$M(r) \;=\; M_0\,[\,\ln(1+\frac{r}{r_s}) \;+\; \frac{1}{(1+\frac{r}{r_s})}\,]. \tag{4}$$

We examine this mass model and its consequences for the resulting dynamics of cluster cores in section 5.

2.3 LENSING BY CLUSTERS

Clusters of galaxies have the optimum cross-section for lensing the nearly isotropically distributed high redshift faint galaxy population. Lensing by an extended mass concentration can be understood in terms of a mathematical mapping (e.g. Blandford & Narayan 1987 and Fort & Mellier 1994) from the source plane onto the image plane with the properties that it conserves surface brightness and is achromatic. The deflections produced are non-linear with impact parameter and therefore produce both amplification and distortion of the background sources. There are two important effects: the isotropic magnification and the non-isotropic distortion. The isotropic magnification is caused by mass interior to the beam and is pronounced in the region of the image plane where the local surface mass density Σ is of the order of the critical surface mass density, $\Sigma_{\rm crit}$, which occurs in the dense cores of rich clusters producing multiple images and arcs. ($\Sigma_{\rm crit}$ depends on the angular distance to the source and lens and hence on cosmological parameters). The anisotropic distortion of images is caused by the gradient of the two-dimensional potential and characterizes the 'weak lensing' regime, the signal being arclets (single weakly sheared images) produced even at large distances from the cluster centre.

A composite mass profile for a cluster can be constructed using a variety of constraints from lensing effects over a range of scales. The strong lensing regime constrains the total mass enclosed within the 'Einstein radius', while weak shear effects (measured statistically from the ellipticities of the faint background galaxies) determine the slope of the mass profile at the outskirts.

2.3.1 Constraints from Strong Lensing

The input from observations for the mass modelling are arc positions, the number of merging images and their parities, and the width, shape and curvature of the arcs. They are used to determine the location of the critical lines in the image plane which are then mapped back to the source plane in the method developed by Kneib (1993). The difference in parameters implied by each of the multiple images is then minimized in the χ^2 sense in the source plane. In order to calibrate the lens model, at least one arc redshift needs to be measured. The usual mass profiles used in modelling the cluster mass distributions are the cored isothermal profile (Blandford & Kochanek 1987), the pseudo-isothermal elliptical mass distribution (PIEMD) (Kassiola & Kovner 1993) or a linear combination of them. The PIEMD model has a 2-D surface mass density defined by:

$$\Sigma(r) = \frac{\Sigma_0}{\sqrt{1+\frac{r^2}{r_0^2}}}, \tag{5}$$

The corresponding 3-dimensional density profile and the mass are,

$$\rho(r) = \frac{\rho_o}{1+\frac{r^2}{r_0^2}}, \tag{6}$$

$$M(r) = M_0\,[\frac{r}{r_0} - \tan^{-1}\frac{r}{r_0}]. \tag{7}$$

Modelling the arcs with this profile, the normalization and the core radius (which is a measure of the compactness of the mass distribution) are determined. The core radius of most lensing clusters is observed to be quite small, $30h_{50}^{-1}\,{\rm kpc} \leq r_o \leq 100h_{50}^{-1}$ kpc.

2.3.2 Constraints from Weak Lensing

The slope of the mass profile at large radii ($r > 200h_{50}^{-1}\,{\rm kpc}$) is constrained by the observed weak distortion effects. The weak shear γ induced by the cluster on the background images can be written for the circularly symmetric case as:

$$\gamma \propto \langle D(z_s)\rangle\,(\bar{\Sigma}(<r) - \Sigma(r)), \tag{8}$$

where $\langle D(z_s)\rangle$ is the mean of the ratio of the angular distances $D_{\rm lens-source}/D_{\rm observer-source}$ and $\bar{\Sigma}$ the mean surface density within radius r. The Kaiser-Squires technique (Kaiser & Squires 1993) defines a mapping that relates the image ellipticities to the relative mass map $\Sigma(r)$ for a cluster. To construct the surface mass density profile one uses the statistic suggested by Fahlman et al. (1994) & Squires et al. (1996),

$$\bar{\Sigma}(<r_1) - \bar{\Sigma}(r_1<r<r_2) = \frac{2\Sigma_{crit}}{1-r_1^2/r_2^2}\int_{r_1}^{r_2}\langle\epsilon_t\rangle\,\frac{dr}{r}, \tag{9}$$

where $\langle\epsilon_t\rangle$ is the mean tangential component of the image ellipticities. For this inversion, deep optical images under exquisite seeing conditions of a wide field over the lensing cluster are required. Details of correction and compensation for the anisotropy of the point-spread function and bad seeing conditions have been demonstrated by Kaiser (1995) and Bonnet & Mellier (1995).

2.3.3 Constraints from the cD galaxy

Dark matter in clusters is sharply peaked about the cluster centre around which the lensed images are seen. In most clusters with spectacular arcs, the centre of the brightest cluster galaxy and the centre of the dark matter distribution as determined both from X-ray and lensing studies seem to be coincident to within the errors - of the order of a few arcseconds.

The central bright elliptical galaxies are often cDs with diffuse halos extending out to beyond the Einstein radius. The orbits of the stars in these halos trace the overall dark matter potential. The density profiles of cD galaxies are fairly well-determined observationally (Kneib et al. 1995) and are best fit by a difference of 2 PIEMD models,

$$\rho(r) = \frac{\rho_0 r_1^2 r_{cut}^2}{(r_{cut}^2-r_1^2)}\,[\frac{1}{r^2+r_1^2} - \frac{1}{r^2+r_{cut}^2}], \tag{10}$$

where r_1 is the core radius and $r_{\rm cut}$ is the truncation radius. The velocity dispersion profile of giant ellipticals is also measured in a number of clusters (Fisher, Illingworth, & Franx 1995) and is found to be, $\sigma_* \sim 300-500\,{\rm km\,s^{-1}}$. Close to the cluster centre, the overall mass profile has to be consistent with the measured isotropic velocity dispersion of stars in the cD (Miralda-Escude 1995).

3 DYNAMICAL EQUATIONS

We model the cluster as a collisionless system in which the individual galaxies move under the influence of the mean gravitational field ϕ generated by all the constituents. The system is characterized by its phase-space density $f(\boldsymbol{x}\,, \boldsymbol{v}\,, t)$, and a given configuration of the system is specified by $f(\boldsymbol{x},\, \boldsymbol{v},\, t)\, d^3\boldsymbol{x}\, d^3\boldsymbol{v}$ – the number of galaxies having positions in the infinitesimal volume $d^3\boldsymbol{x}$, with velocities in the range $d^3\boldsymbol{v}$. It should be noted here that in phase-space $\boldsymbol{x}$ and $\boldsymbol{v}$ are independent variables and the potential is not a function of $\boldsymbol{v}$. The density of points in phase-space satisfies the continuity equation,

$$\frac{Df}{Dt} = \frac{\delta f}{\delta t} + \boldsymbol{v}\,.\boldsymbol{\nabla} f - \boldsymbol{\nabla}\phi.\frac{\delta f}{\delta \boldsymbol{v}} = 0, \tag{11}$$

which is the *collisionless Boltzmann equation*. Neglecting the explicit time derivative; taking the first velocity moment; integrating over all possible velocities for a spherical system, we obtain the *Jeans equation*:

$$\frac{d(\rho\,\sigma_r^2)}{dr} + \frac{\rho\,[2\sigma_r^2 - (\sigma_\theta^2 + \sigma_\phi^2)]}{r} = -\rho\,\frac{d\phi}{dr}, \tag{12}$$

where ρ is the density profile and σ_i^2 are the components of the velocity dispersion. If, additionally, the velocities and the density are invariant under rotations about the cluster centre we have,

$$\sigma_t^2 \equiv \sigma_\theta^2 = \sigma_\phi^2, \tag{13}$$

$$\frac{d(\rho\,\sigma_r^2)}{dr} + \frac{2\beta\,\sigma_r^2\,\rho}{r} = -\rho\,\frac{d\phi}{dr}. \tag{14}$$

The velocity anisotropy parameter β at a given point is,

$$\beta(r) = (1 - \frac{\sigma_t^2}{\sigma_r^2}) \tag{15}$$

3.1 The Isotropic Jeans equation

The isotropic Jeans equation is a special case of the more general equation above, wherein the galaxies are on isotropic orbits. Hence $\beta = 0$, and $\sigma_r^2 = \sigma_t^2$,

$$\frac{d\,(\rho\,\sigma^2\,)}{dr} = -\frac{GM(r)\rho(r)}{r^2} = -\frac{\rho\,v_c^2}{r}, \tag{16}$$

where $v_c(r)$ is defined to be the circular velocity. The solutions for the isotropic velocity dispersion are given by:

$$\sigma^2(R) = \frac{G}{\rho}\int_R^\infty \frac{M(r)\rho(r)\,dr}{r^2} = \frac{1}{\rho}\int_R^\infty \rho(r)\,v_c^2(r)\,\frac{dr}{r}. \tag{17}$$

The velocity dispersion of both the galaxies and the total mass can therefore be computed given their respective density profiles and the underlying mass distribution. We plot the solutions obtained for a mass model of the form,

$$M(r) = M_0\,[\frac{r}{r_0} - \tan^{-1}\,\frac{r}{r_0}], \tag{18}$$

with $r_0 = 50\,\mathrm{kpc}$, $\sigma_0 = 1200\,\mathrm{km\ s^{-1}}$, and generic density profiles for the tracers (galaxies or isothermal gas) of the form,

$$\rho(r) = \frac{\rho_o}{(1 + \frac{r^2}{r_c^2})^\alpha}. \tag{19}$$

The solutions for $\alpha = 1.0$, 1.2 and 1.5 and for various values of $r_c/r_0 = 1.0$, 2.5 and 5.0 are plotted in Fig. 1. The solutions have the following interesting properties:

(i) the velocity dispersion falls in the centre for small core radii,
(ii) the smaller the core radius of the tracer, the lower the central value of the velocity dispersion,
(iii) the mean value of the velocity dispersion is a weak function of r_c but depends on the slope α.

Therefore one can have different mean values of the velocity dispersion for different components if they do not have the same radial profile.

In Fig. 1, we also plot the ratio of the velocity dispersions of dark matter and galaxies, which provides a qualitative understanding of the velocity bias (as found in the numerical simulations by Carlberg 1994). The difference in the asymptotic slope of the density profiles of dark matter and galaxies, and the ratio of the core radii is found to determine the velocity bias. To first order, the asymptotic behavior (regardless of core size) is:

$$\left(\frac{\sigma_{DM}}{\sigma_g}\right)^2 \simeq \frac{\alpha_{DM}}{\alpha_g} \tag{20}$$

3.2 Anisotropic Jeans equation

The Jeans equation is a mathematical statement of detailed pressure balance for an equilibrium stellar system. The dynamical evolution of clusters in N-body simulations has been studied using the distribution function formalism (Natarajan, Hjorth, & Van Kampen 1996). This analysis indicates that clusters evolve from one quasi-equilibrium state to another. A cluster in a quasi-equilibrium configuration is found to be virialized and has a smooth potential, which is traced by galaxies with one of the following orbital structures :

(i) $\beta = 0$, isotropic orbits
(ii) $0 < \beta \leq 1$, orbits are mostly radial
(iii) $\beta < 0$, when the orbits are primarily transverse.

While β has no lower bound, it is strictly required to be less than 1 for any physically admissible solutions for the velocity dispersion. In this context, it is instructive to examine and compare with studies of the formation and evolution of elliptical galaxies (Hjorth & Madsen 1991). It has been shown that the observed uniformity in the properties of elliptical galaxies can arise from either of two sets of initial conditions: dissipationless cold collapse or a 'warm collapse' (or merger) with dissipation. The predicted evolution to the final state with a deep potential and significant radial anisotropy arises from the relaxation brought about by global potential fluctuations rather than two-body encounters (Aguilar & Merritt (1990) and Londrillo, Messina, & Stiavelli (1991)). Therefore, radial anisotropy can arise naturally in most models as a consequence of relaxation, and as demonstrated by Gerhard (1993) the line-of-sight velocity profiles being more sensitive to β and less so to the potential or to the stellar number density profile provide a probe of the kinematics of the core. Conversely, for a galaxy cluster, the initial collapse conditions are different and additionally, many physical processes that can effect energy exchange are

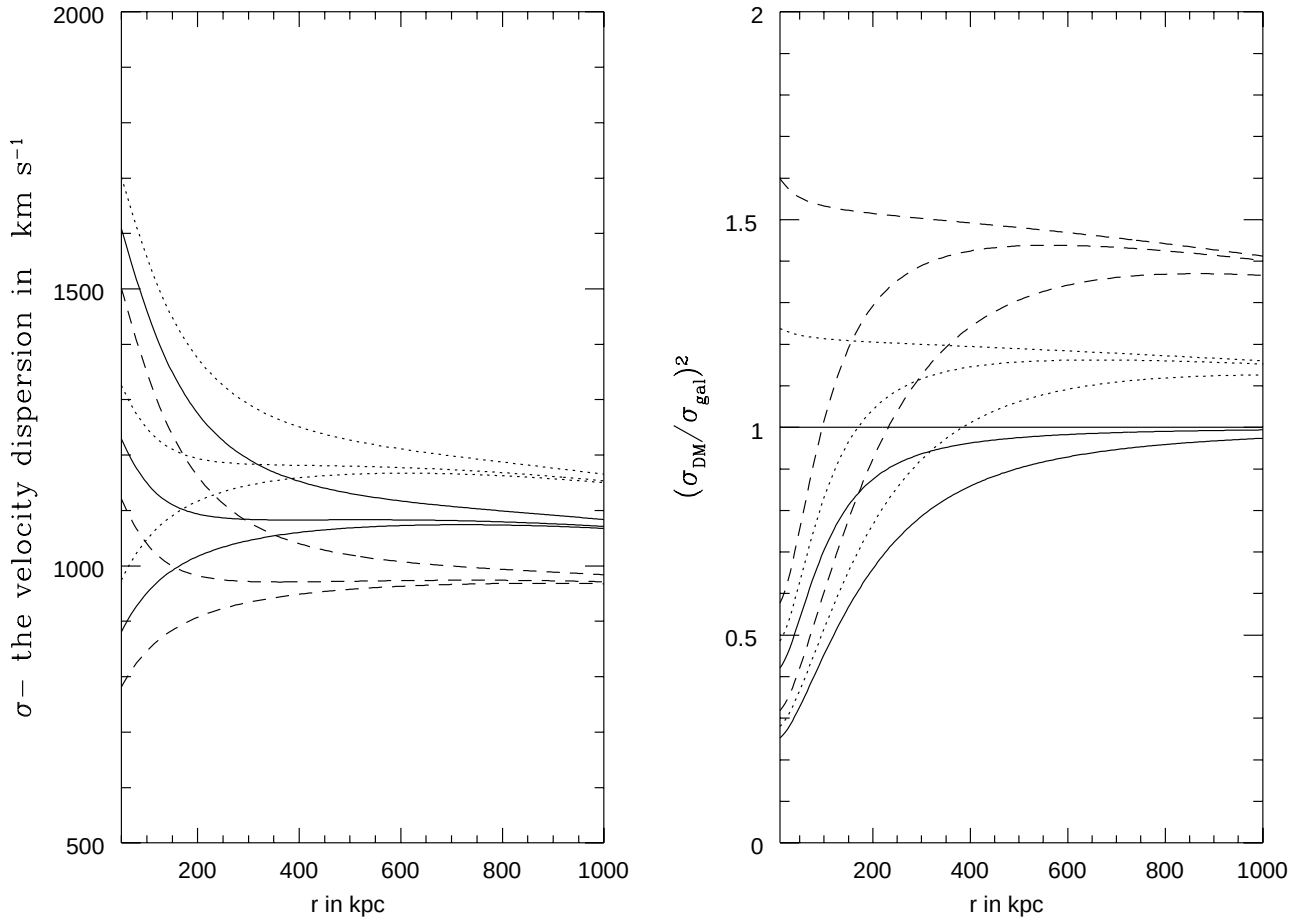

Figure 1. Left panel: Solutions of the isotropic Jeans equation. The dotted curves are for $\alpha = 1.0$, dashed curves for $\alpha = 1.2$ and solid curves for $\alpha = 1.5$; for each α, the smaller the core radius for the tracer, the smaller the central velocity dispersion (see text). Right panel:Ratio of the velocity dispersions for various values of α and core radius r_0: solid curves - $\alpha_{DM}/\alpha_{gal} = 1.0$, $r_g = 50$, 125 and 250 kpc; dotted curves - $\alpha_{DM}/\alpha_{gal} = 1/1.2$, $r_g = 50$, 125 and 250 kpc; dashed curves - $\alpha_{DM}/\alpha_{gal} = 1/1.5$ for $r_g = 50$, 125 and 250 kpc

active and do occur in the dense core region. For a cluster core that has virialized, we expect the orbits in the core to reflect the efficiency of the energy exchange mechanisms, while outside the core region, we expect and do find that the orbits are largely radial, $0 < \beta \leq 1$ (Natarajan, Hjorth, & Van Kampen 1996).

4 PROPOSED APPROACH

4.1 THE MATHEMATICAL FORMALISM

In our approach, we solve the full Jeans equation for the velocity anisotropy parameter β and for the radial component of the velocity dispersion σ_r^2, using the projected mass profile for the cluster as constructed independently from gravitational lensing.

From the observed projected galaxy positions, we fit to get a surface number density profile $\Sigma_g(r)$ and use the Abel integral inversion to extract the three-dimensional density profile $\nu_g(r)$. The key assumption made in the analysis below is that of spherical symmetry. Starting with the full Jeans equation,

$$\frac{d\,(\nu_g\,\sigma_r^2)}{dr} + \frac{2\beta(r)\nu_g\ \sigma_r^2}{r} = -\frac{G\ M_{\rm tot}(r)\nu_g}{r^2}; \tag{21}$$

where $\nu_g(r)$ is three-dimensional galaxy density profile, $\sigma_r^2(r)$ the radial velocity dispersion of the galaxies, $\beta(r)$ is the velocity anisotropy and $M_{\rm tot}(r)$ is the distribution of total mass (most accurately determined from gravitational lensing).

In addition, we have the equation that defines the observed line-of-sight velocity dispersion profile $\sigma_{los}(R)$,

$$\frac{1}{2}\,[\,\Sigma_g(R)\,\sigma_{los}^2(R)] \,=\, \int_R^\infty \frac{r\nu_g(r)\sigma_r^2(r)\,dr}{\sqrt{(r^2-R^2)}} \\ -R^2\int_R^\infty \frac{\beta(r)\sigma_r^2(r)\nu_g(r)\,dr}{r\sqrt{(r^2-R^2)}}. \tag{22}$$

We need to solve these two integro-differential equations numerically for σ_r^2 and $\beta(r)$. For an individual galaxy with an

assumed mass profile, these coupled equations have been solved by Binney (1982) and Bicknell et al. (1989).

We truncate the integration at a large, finite truncation radius R_t, defined strictly to be the radius at which both $\Sigma_g(R_t)$ and $\rho_g(R_t)$ tend to zero. Substituting the expression for β from equation (22) we have,

$$\frac{1}{2}[\ \Sigma_g(R)\ \sigma^2_{los}(R) - \ R^2 \int_R^{R_t} \frac{GM_{\rm tot}(r)\nu_g}{r^2\sqrt{r^2-R^2}}\, dr] = \int_R^{R_t} \frac{r\nu_g\sigma_r^2 dr}{\sqrt{r^2-R^2}} + \frac{R^2}{2}\int_R^{R_t} \frac{d(\nu_g\sigma_r^2)}{dr}\frac{dr}{\sqrt{r^2-R^2}}. \quad (23)$$

Integrating the first term on the right hand side by parts and substituting back we have,

$$\frac{1}{2}[\Sigma_g(R)\sigma^2_{los}(R) - R^2\int_R^{R_t} \frac{GM_{\rm tot}(r)\nu_g}{r^2\sqrt{r^2-R^2}}dr] = \int_R^{R_t} \frac{(\frac{3R^2}{2}-r^2)}{\sqrt{r^2-R^2}}\frac{d(\nu_g\sigma_r^2)}{dr}\, dr. \quad (24)$$

The equation can be further simplified and reduced after some algebra (for details see Bicknell et al. 1989) to the following integrals,

$$\nu_g(r)\sigma_r^2 = I_1(r) - I_2(r) + I_3(r) - I_4(r), \quad (25)$$

$$I_1(r) = \frac{1}{3}\int_r^{R_t} \frac{GM_{\rm tot}(r)\,\nu_g}{r^2}\, dr, \quad (26)$$

$$I_2(r) = \frac{-2}{3r^3}\int_0^r GM_{\rm tot}(r)\,\nu_g\, r\, dr, \quad (27)$$

$$I_3(r) = \frac{1}{r^3}\int_0^r R\ \Sigma_g(R)\sigma^2_{los}(R)\, dR, \quad (28)$$

$$I_4(r) = \frac{2}{\pi r^3}\int_r^{R_t} R\ \Sigma_g(R)\,\sigma^2_{los}(R)[\ \frac{r}{\sqrt{R^2-r^2}} - sin^{-1}\frac{r}{R}\ ]\, dR. \quad (29)$$

It is to be noted here that the explicit dependence on the mass profile and the observed line-of-sight velocity dispersion profile separate. All the above integrals are well-behaved with the exception of I_4, which has an integrable singularity which can be taken care of easily via a simple transformation of variables. Computing these integrals is nevertheless tricky as the final profile for $\sigma_r^2(r)$ is sensitive to the precise asymptotic behavior of all the four terms. The numerical solution for $\sigma_r^2(r)$ is then substituted back into the Jeans equation to obtain β,

$$\beta(r) = -\frac{r}{2\nu_g\sigma_r^2}\,[\ \frac{GM_{\rm tot}(r)\,\nu_g}{r^2} + \frac{d}{dr}(\rho_g\sigma_r^2)\ ]. \quad (30)$$

The variation of β with radius can be understood physically in terms of the relative importance of the mass term and the 'galaxy pressure' gradient term. Rewriting the above equation as follows,

$$\beta(r) = -\frac{1}{2}\,[\ \frac{v_c^2(r)}{\sigma_r^2(r)}\ +\ \frac{d\,\ln\,\nu_g\,\sigma_r^2}{d\,\ln\,r}\ ] \quad (31)$$

we find that the sign of β depends crucially on the asymptotic behavior of the mass model at large r, and specifically for $\rho_{\rm tot}$ ranges between r^{-2} and r^{-3}, it is found to be fairly insensitive to the slope of the assumed galaxy density profile. The sensitivity of the sign and magnitude of β to the slope of the mass profile enables its use as a discriminant between the various mass models.

5 RESULTS FOR VARIOUS MASS PROFILES

We consider several physically motivated fiducial density profiles for the total mass and in what follows, we examine both galaxy distribution profiles described in equation (1) (PROFILE A) and equation (2) (PROFILE B). The asymptotic slope of the density profile is defined to be γ. All the mass profiles are normalized to have the same total projected mass enclosed within the Einstein radius $[M_{arc}(r_E = r_{arc}) = (5 \pm 0.1) \times 10^{13}\, M_\odot]$, as calibrated from strong cluster lensing in A2218. The density profiles and mass models studied are:

MODEL I :

$$\rho(r) = \frac{\rho_0}{r(r^2+r_0^2)^\alpha}\ ;\ \gamma = 2\alpha + 1, \quad (32)$$

$$M(r) = 2\pi\rho_0\ \ln\,(\mathrm{r}^2 + \mathrm{r}_0^2)\ ;\ \alpha = 1. \quad (33)$$

MODEL II :

$$\rho(r) = \frac{\rho_0}{(r^2+r_0^2)^\alpha}\ ;\ \gamma = 2\alpha, \quad (34)$$

$$M(r) = 4\pi\rho_0 r_0\,[(\frac{r}{r_0}) - tan^{-1}(\frac{r}{r_0})]\ ;\ \alpha = 1. \quad (35)$$

MODEL III :

$$\rho(r) = \frac{\rho_0}{r(r+r_0)^\alpha}\ ;\ \gamma = \alpha + 1, \quad (36)$$

$$M(r) = 4\pi\rho_0 r_0\,[\,\frac{r}{r_0} - \ln\,(\mathrm{r} + \mathrm{r}_0)\,]\ ;\ \alpha = 1. \quad (37)$$

5.1 Dependence on the slope γ

We analyse here the results for the various mass models with a specified asymptotic slope γ, assuming a core radius of $r_g = 250\,$kpc for the galaxy distribution of PROFILE A with $r_0 = 60\,$kpc for the dark matter.

(i) For $\gamma = -2.0$ (Fig. 3 - top panel), and a range of input values of the line of sight velocity dispersion assumed to be constant ($\sigma_{los} = 800$, 1000, *and* $1400\,$km s^{-1}); we obtain unphysical solutions ($\sigma_r(r) < 0$) for the lowest σ_{los} for all the 3 models. On increasing σ_{los} to $1000\,$km s^{-1}, the orbits are primarily transverse in the core progressing to more radial ones in the outer parts, so that $\beta < 0$. For the highest σ_{los} we find evidence for a small core region with mixed orbits, but with primarily radial orbits outside 200 kpc for all 3 models.

(ii) For $\gamma = -2.5$ (Fig. 3 - middle panel), unphysical solutions are obtained for the lower σ_{los} value for all models, but for $\sigma_{los} = 1000$ *and* $1400\,$km s^{-1} we do find physically admissible solutions. All 3 mass models have a finite core with mixed orbits leading on to largely radial orbits outside. Model I has the largest mixed region (of the order of 700 kpc)

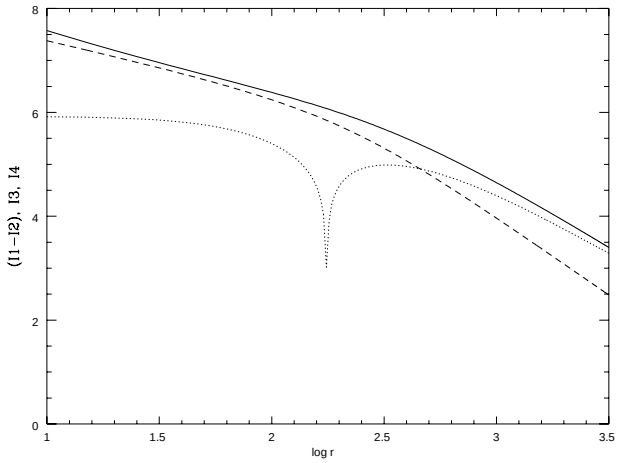

Figure 2. The Integrals - (I1-I2) - dotted curve, I3 - dashed curve, I4 - solid curve, computed for A2218.

while Models II and III have smaller mixed regions which are of the order of 500 kpc. The highest value of σ_{los} produces primarily radial orbits from the centre outward.

(iii) For $\gamma = -3.0$ (Fig. 3 - bottom panel), and the lowest value of σ_{los}, we obtain unphysical solutions, but as σ_{los} is increased there is evidence for a core with transverse orbits.

Assuming the galaxy distribution to be of the form of PROFILE B with a scale radius $s = 200\,\mathrm{kpc}$ and $r_0 = 60\,\mathrm{kpc}$ for the dark matter, we find the following trends:

(i) For $\gamma = -2.0$ (Fig. 4 - top panel), and the same range of input values of the line of sight velocity dispersion ($\sigma_{los} = 800$, 1000, *and* $1400\,\mathrm{km\ s^{-1}}$), we obtain unphysical solutions in the core region for the lowest σ_{los} for all the 3 models. On increasing σ_{los} to $1000\,\mathrm{km\ s^{-1}}$, the orbits tend to be tranverse so that $\beta < 0$. For the highest σ_{los} we find primarily radial orbits for all 3 models.

(ii) For $\gamma = -2.5$ (Fig. 4 - middle panel), unphysical solutions are obtained for the lower σ_{los} value for all models, but for $\sigma_{los} = 1000$ we find that all 3 mass models have a finite core (of the order of 500 kpc) with mixed orbits leading on to largely radial orbits outside. The highest value of σ_{los} produces primarily radial orbits right from the centre outward.

(iii) For $\gamma = -3.0$ (Fig. 4 - bottom panel), once again for the lowest value of σ_{los}, we obtain unphysical solutions, but as σ_{los} is increased there is evidence for a core with tangential anisotropy.

Both PROFILES A and B require high values of the line-of-sight velocity dispersion to produce physically meaningful solutions. The trends above seem to be qualitatively consistent with the physical picture of ongoing isotropization and regularization in the core for all the 3 fiducial mass models considered.

5.2 Dependence on the circular velocity

An important parameter for the dynamics of the galaxies in the global cluster potential is the circular velocity, v_c (Fig. 4), which measures the change in slope of the mass profile. For a given mass model with asymptotic slope γ, increasing the core radius increases the circular velocity for all three models (where these were normalized to have the same projected mass within the radius of the arc).

Comparing different mass models that have the same asymptotic value of v_c (but different r_0 and γ), we find that the velocity structure of the core and anisotropy profiles are fairly similar. The qualitative behavior of β for fixed asymptotic v_c depends strongly on σ_{los}; with increasing σ_{los} we find preferentially radial orbits. For a fixed σ_{los}, increasing the circular velocity increases the size of the mixed core region while lowering the value of β at large radius. For both high and low circular velocities, and $-3.0 \leq \gamma \leq -2.0$; low line-of-sight velocity dispersion models $\sigma_{los} < 1000\ \mathrm{km\ s^{-1}}$ are ruled out purely from the dynamical point of view.

5.3 Dependence on the central density profile

The best probe of the shape of the density profile at the very centre comes from the observed velocity dispersion of the stars in the cD halo (Miralda-Escude 1995). For the fiducial mass models of Section 5, we solve for the line-of-sight velocity dispersion of the cD halo stars using the isotropic Jeans equation (neglecting the contribution of the mass of the cD galaxy to the total mass of the cluster):

$$\frac{d\,(\rho_{cD}\,\sigma_*^2\,)}{dr} = -\frac{GM_{\rm tot}(r)\rho_{cD}}{r^2}. \tag{38}$$

Assuming a scaling of $\rho_{cD} \propto r^{-\delta}$, and $\rho_{tot} \propto r^{-\gamma}$, close to the centre we obtain:

$$\sigma_* = A\,\frac{r^{2-\gamma}}{(\delta+\gamma-2)} + const. \tag{39}$$

Therefore, for $0 \leq \gamma < 2$ and $\delta + \gamma > 2$, we expect the velocity dispersion of the stars to rise. The cD profile from section 2.3.4 is used with a core radius $r_1 = 0.05\,\mathrm{kpc}$ and $r_{cut} = 35.0\,\mathrm{kpc}$. The three models studied in the previous section, predict profiles (Fig. 5) with low central values for σ_* that rise steeply with radius. Models I and III have central values $\sim$ 200 - 400 km s^{-1}, varying with γ, such that the steeper the total mass profile the higher the central value.

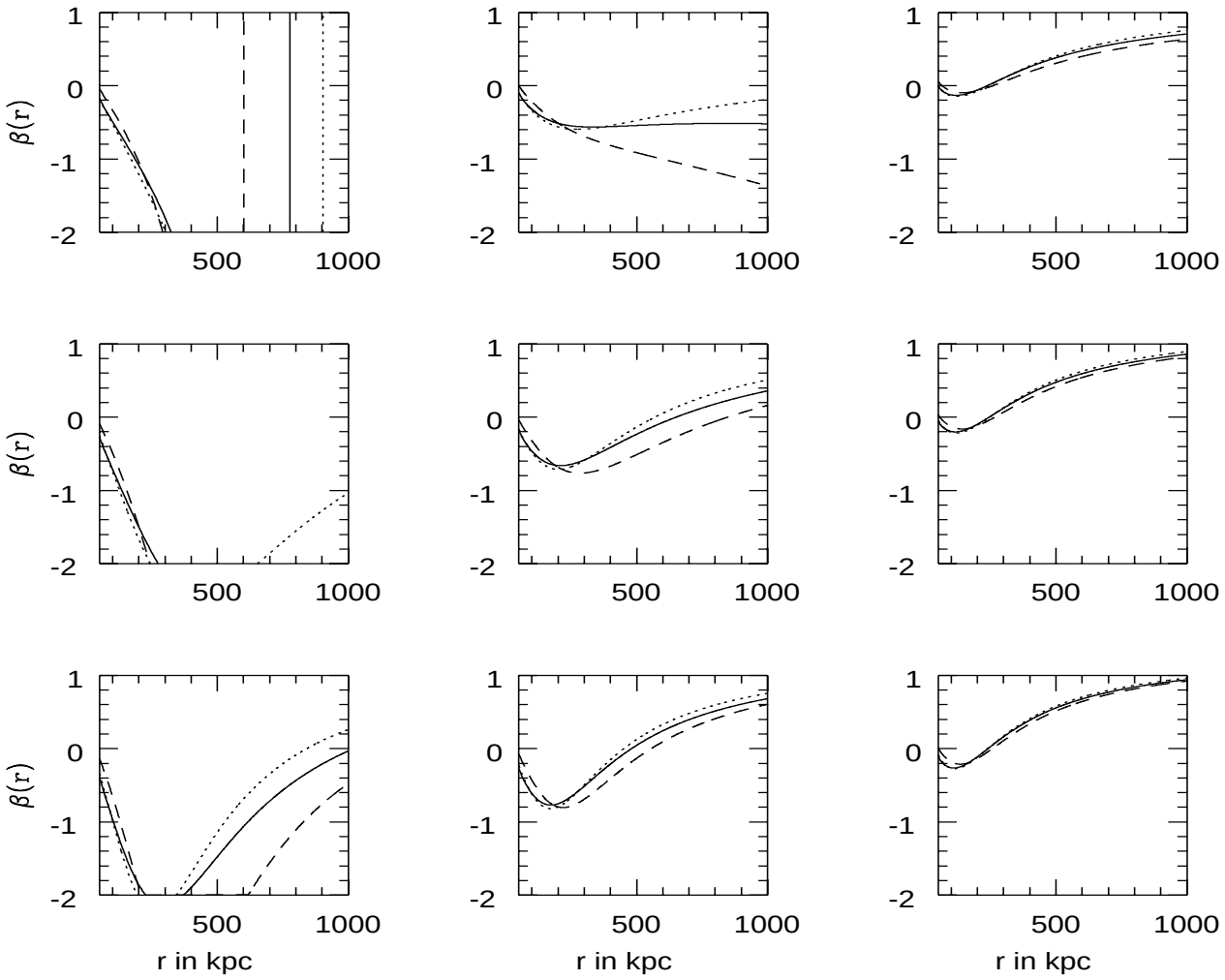

Figure 3. Top Panel: $\beta(r)$ for PROFILE A with r_g = 250 kpc, the mass models with asymptotic slope γ = -2.0; solid curve - Model I, dotted curve - Model II, dashed curve - Model III, for σ_{los} = 800, 1000 and 1400 km s^{-1} respectively. Centre Panel: $\beta(r)$ For the mass models with asymptotic slope γ = -2.5; solid curve - Model I, dotted curve - Model II, dashed curve - Model III, for σ_{los} = 800, 1000 and 1400 km s^{-1} respectively. Bottom Panel: $\beta(r)$ For the mass models with asymptotic slope γ = -3.0; solid curve - Model I, dotted curve - Model II, dashed curve - Model III, for σ_{los} = 800, 1000 and 1400 km s^{-1} respectively.

For the stars, σ_{los} rises to 700 km s^{-1} at $r = 100\,$kpc, which is consistent with the measurements of the cD galaxy IC1011 in A2029 by Dressler (1979) and Fisher, Illingworth, & Franx (1995). Model II under-predicts the central value and is qualitatively incompatible with the data.

5.4 Summary of the important parameters

In the above analysis, there are several parameters to be kept track of in order to interpret the results for the computed velocity structure of the cluster core, namely the total mass distribution and the galaxy positions and velocities.

The mass profile for a given fiducial model is specified by three parameters, the central density, the core radius, and the slope. The velocity dispersion of stars in the cD halo favors mass models with a central 'cusp'. Lensing constrains (i) the mass within the radius of the arc (strong regime), (ii) the circular velocity at large radius (weak-shear), and the generic shape of the profile. It favors compact cores and rules out steep slopes, $\gamma < -2.5$ for $50 \leq r \leq 600\,$kpc. Our results show that the dynamics of the core can be recovered independent of the fine tuning of individual fiducial models, given the above constraints from lensing and an observationally well-determined line-of-sight velocity dispersion profile. Although currently limited by the errors in the observationally determined input quantities, this dynamical approach offers a better understanding of the physical state of the cluster core and can discriminate between various mass models for an individual lensing cluster.

6 APPLICATION TO A2218

We apply this technique to the Abell cluster A2218, at a redshift $z = 0.175$, with a mean measured velocity disper-

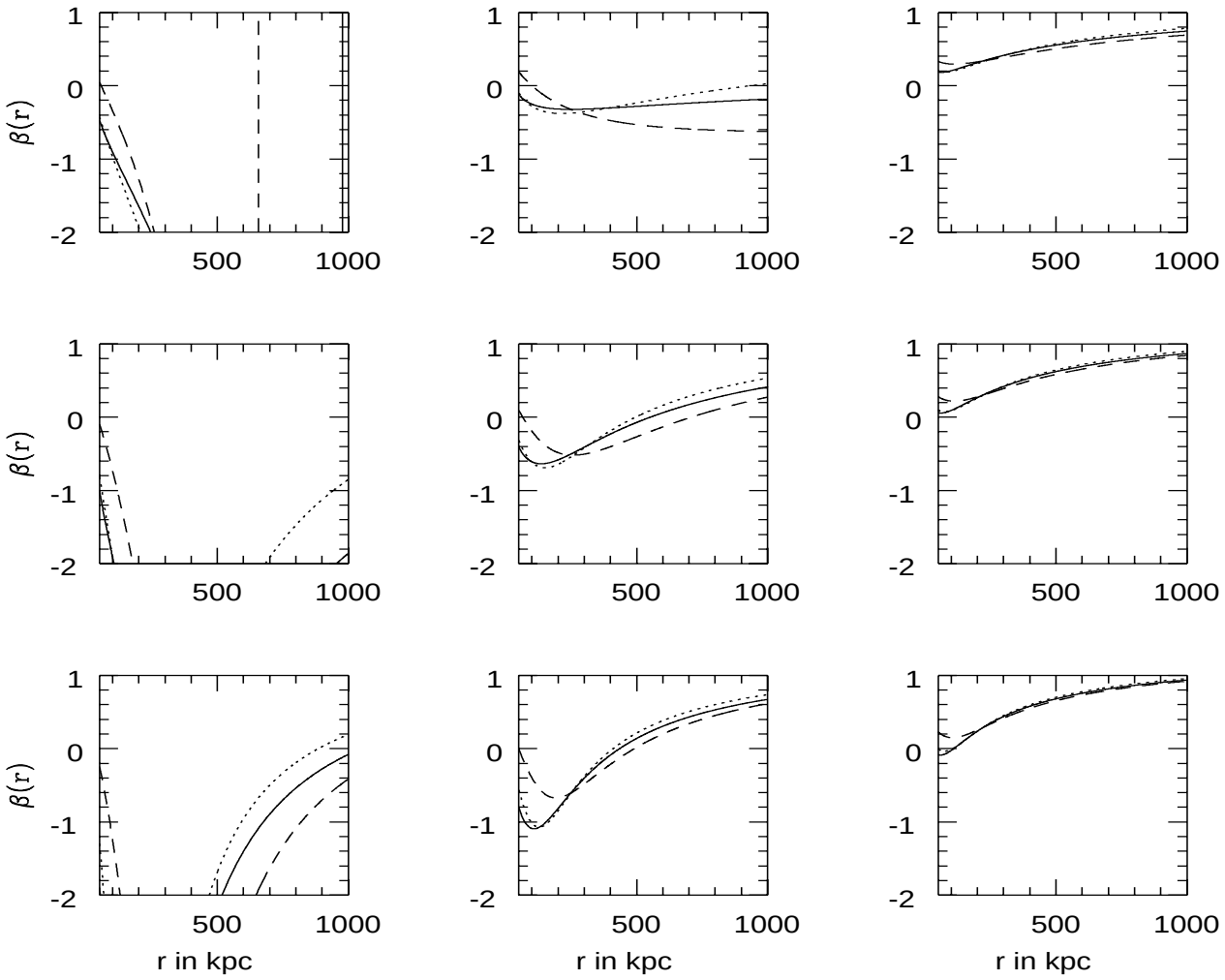

Figure 4. Top Panel: $\beta(r)$ for PROFILE B with s = 200 kpc, the mass models with asymptotic slope γ = -2.0; solid curve - Model I, dotted curve - Model II, dashed curve - Model III, for σ_{los} = 800, 1000 and 1400 km s^{-1} respectively. Centre Panel: $\beta(r)$ For the mass models with asymptotic slope γ = -2.5; solid curve - Model I, dotted curve - Model II, dashed curve - Model III, for σ_{los} = 800, 1000 and 1400 km s^{-1} respectively. Bottom Panel: $\beta(r)$ For the mass models with asymptotic slope γ = -3.0; solid curve - Model I, dotted curve - Model II, dashed curve - Model III, for σ_{los} = 800, 1000 and 1400 km s^{-1} respectively.

sion $\sigma_{mean} \sim 1370^{+160}_{-120}$ km s^{-1} from 56 cluster members. A2218 is a cD cluster with a very peaked mass distribution and a compact core, hence a large number of gravitationally distorted arcs and arclets are observed. The mass model for this cluster was constructed using ground data (Kneib et al. 1995) and refined using HST data by (Kneib et al. 1996). Redshifts of two of the arcs were spectroscopically measured by Pello et al. (1992) and further redshifts of arclets have been determined by Ebbels et al. (1996) hence tightly calibrating the mass model.

6.1 OBSERVATIONAL DATA

The observational input for the galaxies in A2218 for our analysis comes primarily from the photometric and spectroscopic survey by Le Borgne, Pelló, & Sanahuja (1992).

6.1.1 Line-of-Sight Velocity Dispersion Profile

In order to construct the line-of-sight velocity dispersion profile (Fig. 6), the galaxies were binned in 100 kpc annuli. The measurement errors preclude any fitting, and therefore we assumed a constant value for σ_{los}. This simplifying assumption is the largest source of error for our present analysis, but can be refined with the availability in the near future of more tightly sampled line-of-sight velocity dispersion profiles.

6.1.2 Galaxy density profile from optical data

The observed surface density of galaxies in A2218 was fitted to a modified Hubble law profile (PROFILE A) with a core radius $r_g = 250\,h_{50}^{-1}$ kpc,

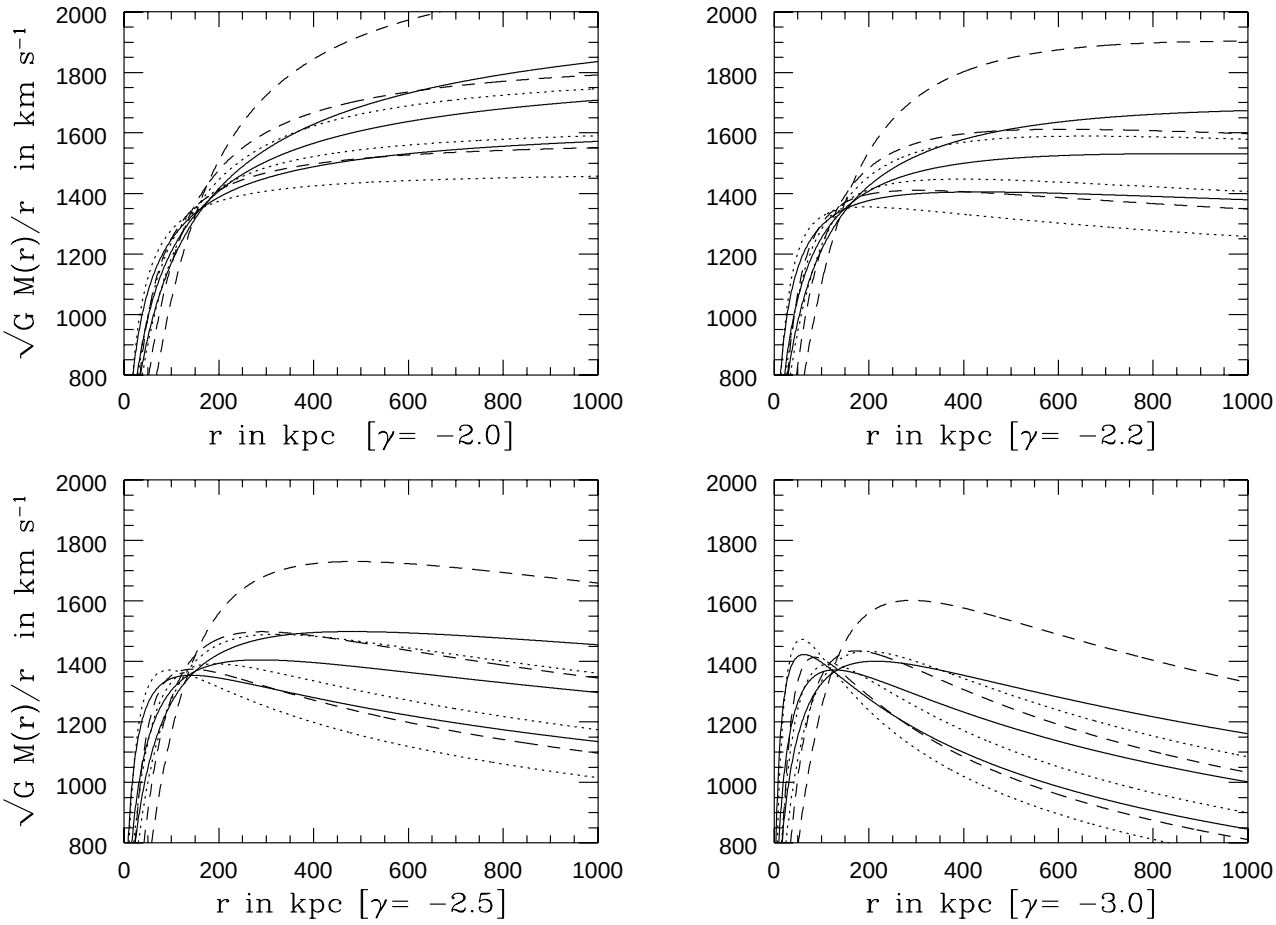

Figure 5. Asymptotic behavior of the fiducial mass models - varying the core radius $r_0 = 30$, 60, 100 kpc; solid curves - Model I, dotted curves - Model II, dashed curves - Model III

$$\Sigma_g(r) = \frac{\Sigma_0}{1+\frac{r^2}{r_g^2}}, \tag{40}$$

and the corresponding 3-D density profile from equation (1), as well as by the cuspy profile (PROFILE B) with a scale radius $s = 200\,h_{50}^{-1}$ kpc,

$$\Sigma_g(r) = \frac{\Sigma_0}{(\frac{r}{s})^{0.1}(1+\frac{r}{s})^{1.9}} \tag{41}$$

and the corresponding density profile from equation (2).

6.1.3 Constructing the mass profile

The lensing mass profile for the cluster was constructed from, the strong lensing data (arcs, arclets and resolved multiple images) from ground-based observations and the HST image by (Kneib et al. 1996), and the weak-lensing mass map published by Squires et al. (1996).

A2218 is best fit by the following functional form of MODEL III with $\alpha = 1.0$ (see Section 5),

$$M(r) = M_0[\frac{r}{r_0} - \ln(1+\frac{\mathrm{r}}{\mathrm{r_0}})], \tag{42}$$

where we normalize M_0 to the mass enclosed by the arc at $r_{arc} = 78.5\,h_{50}^{-1}$ kpc and r_0 the core radius is $60h_{50}^{-1}$ kpc. The corresponding three-dimensional density profile is as below,

$$\rho(r) = \frac{\rho_0 r_0^2}{r(r+r_0)}, \tag{43}$$

with $\rho_0 = 1\cdot 10^{-22}$ g cm^{-3}. The X-ray mass profile was obtained using the standard deprojection technique described by Fabian et al. (1981) to the archival ROSAT HRI map, assuming spherical symmetry and hydrostatic equilibrium for the intracluster gas. The integrated X-ray luminosity (in the 0.1 – 2.4 keV band) and central temperature of A2218 are measured to be respectively,

$$L_x = 7.10^{44}\ erg\ s^{-1}\ ;\ T = 8\,keV, \tag{44}$$

in good agreement with the Squires et al. (1996) results. The predicted circular velocity is,

$$v_c^2(r) = \frac{G\,M(r)}{r} = -\frac{kT}{\mu m_p}(\frac{d(\ln\rho_{\rm gas})}{d\ln r} + \frac{d\ln \mathrm{T}}{d\ln \mathrm{r}}) \tag{45}$$

where $M(r)$ is the total mass as inferred from the X-ray analysis,

The mass model from N-body simulations was also normalized to the mass enclosed within the Einstein radius, and for consistency with the observed arcs in A2218 the scale

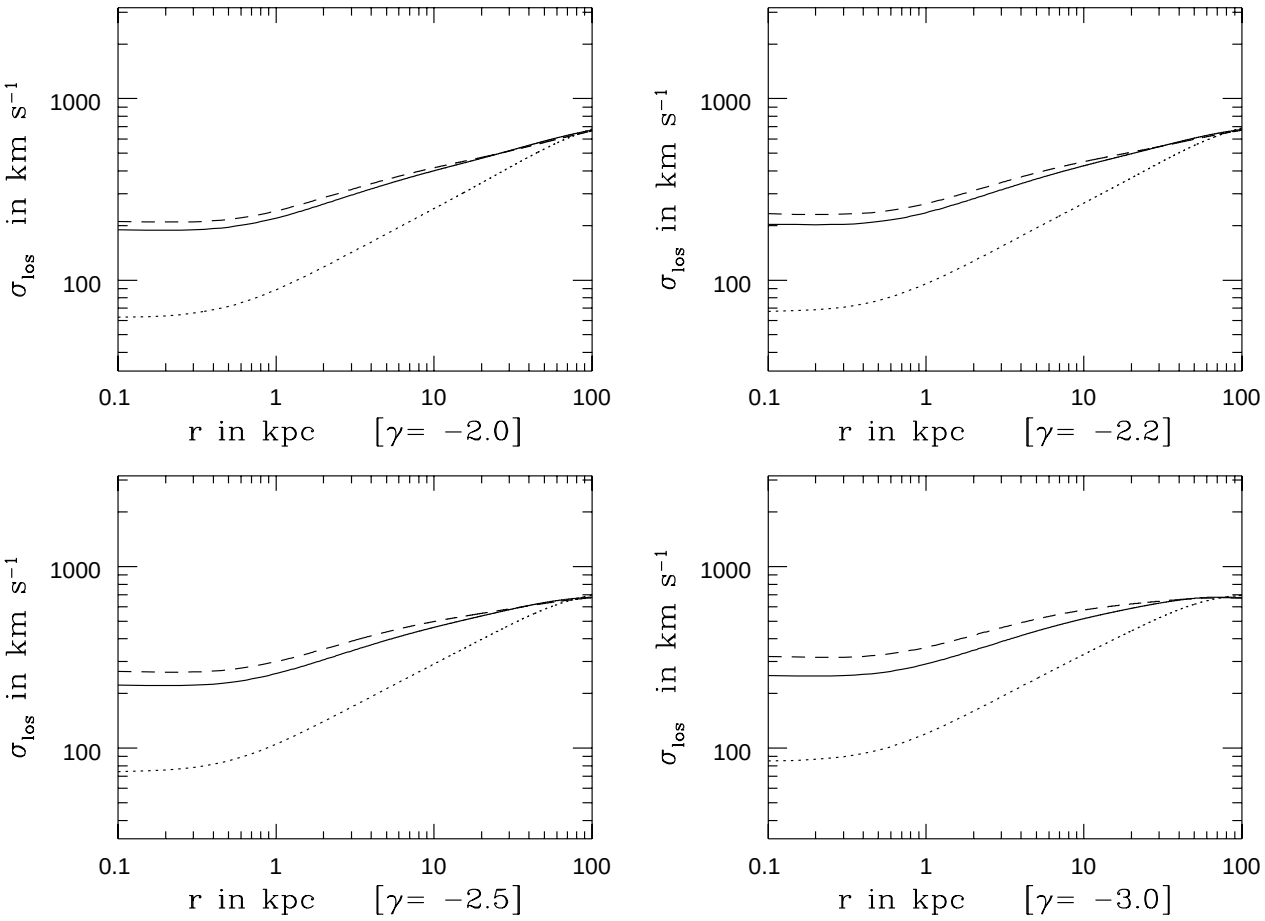

Figure 6. Computed line-of-sight velocity dispersion for the cD halo stars: solid curve - Model I, dotted curve - Model II, dashed curve - Model III.

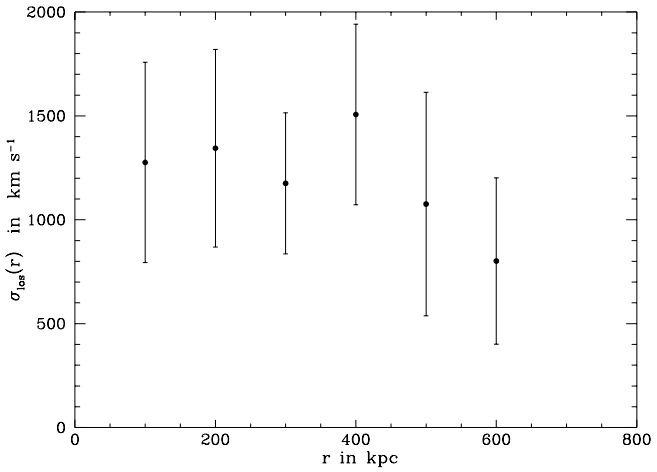

Figure 7. The line-of-sight velocity dispersion profile for A2218

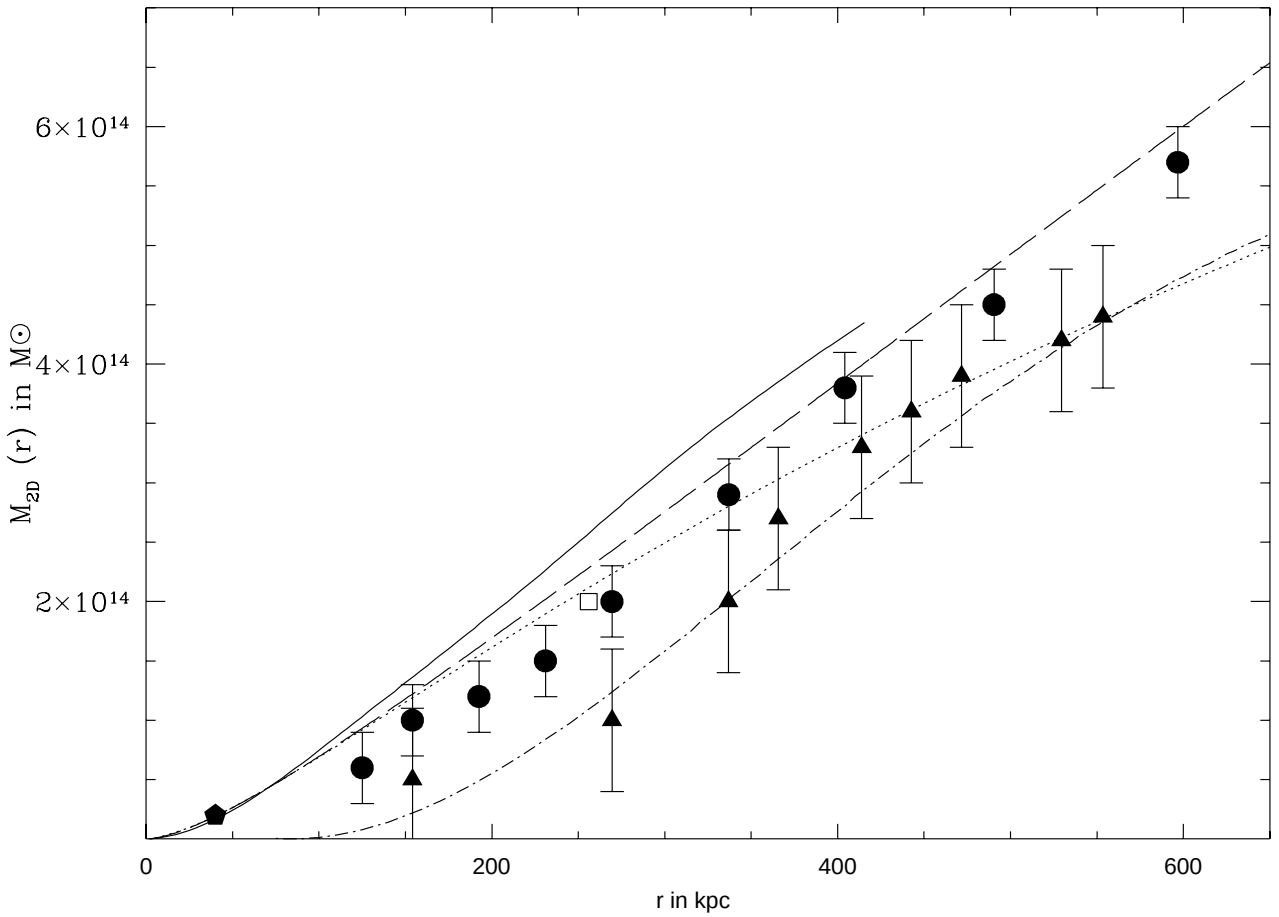

Figure 8. Projected mass profile: solid triangles - X-ray data, solid circle - weak lensing mass estimates, filled pentagon - mass from cD, filled square - mass enclosed within giant arc, solid line - HST mass model, dashed line - 'best fit' composite lens mass model, dot-dashed - fitted X-ray mass model, dotted line - 'best fit' N-body model.

radius r_s (see equation 3) is required to be of the order of $250\,h_{50}^{-1}$ kpc (Waxman & Miralda-Escudé 1995).

6.2 Results

Using the total mass profile constructed from lensing as described above, we solve the equations to obtain solutions (see Fig. 8) for $\sigma_r(r)$, $\sigma_t(r)$ (the radial and transverse velocity dispersion profiles respectively) and the velocity anisotropy parameter $\beta(r)$.

The profile was also checked for consistency with the measured stellar velocity dispersion of the halo stars in the cD galaxy (Fig. 9). [It is to be noted here that the measured line-of-sight velocity dispersion profile for A2218 is inconsistent with an isotropic solution.] We find that the orbits predicted for the best-fit mass model in the central regions, isconsistent with the picture of a core not in equilibrium, independent of the assumed form for the galaxy number density distribution. The precise nature of orbits *transverse* ($\beta < 0$) or *radial* ($0 > \beta > 1$) depends on the detailed shape of the line-of-sight velocity dispersion profile, which is not measured to adequate precision at present. Both σ_r and σ_t fall within the inner $600\,h_{50}^{-1}$ kpc, with σ_r declining more rapidly and then tending to flatten off. From the slope of β, the trend with increasing r is that the nature of orbits tends to being mainly radial at the outskirts, signaling the existence of a region dominated by infall. The physical picture that emerges for the description of the dynamical state of A2218 is one of a dynamically disturbed cluster core. For lower values of the measured line-of-sight velocity dispersion, we find a tendency for the predominance of transverse orbits in the central 400 kpc (which is precisely of the order of the distance between the 2 distinct optical clumps seen in the HST image) and could be interpreted as an indication of on-going energy exchange in the core. Using the mass model from N-body simulations as the input, we find that the resultant predictions for $\beta(r)$ agree well with those calculated for the mass profile reconstructed from lensing. For the mass profile from X-ray data for A2218, we obtain qualitative agreement with the predictions from the lensing mass model.

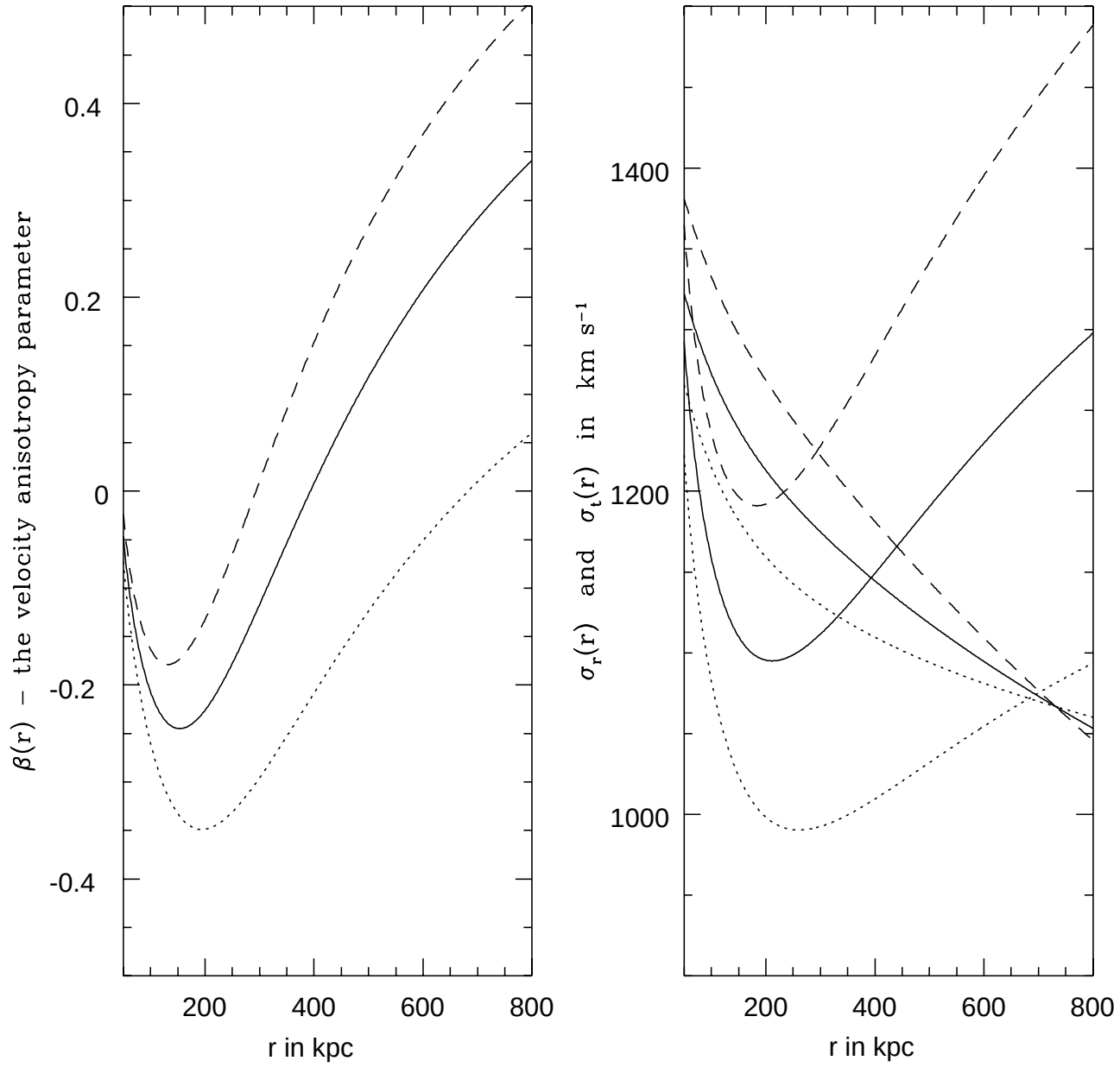

Figure 9. The best fit composite mass model for A2218 : The radial and transverse components of the velocity dispersion and the velocity anisotropy parameter for σ_{los} = 1100, 1200, 1300 km s^{-1} and the galaxy distribution modeled by PROFILE A with $r_g = 250\,h_{50}^{-1}$ kpc,

7 CONCLUSIONS

Gravitational lensing provides the 'cleanest' way to construct the total mass profile for a cluster independent of the kinematic details; additionally, combining strong and weak lensing removes the scaling ambiguity allowing the calibration of other independent mass models. With 'good' data for an individual cluster, the requirements for consistency on the smallest to the largest scales are stringent enough to constrain the slope of generic density profiles for rich clusters. Accurate mass profiles are crucial to settling many important issues such as the baryon fraction problem and in understanding the discrepancies and biases arising in the X-ray, lensing and virial mass estimates for clusters.

In this paper, we have demonstrated that the dynamics and velocity structure of the core of galaxy clusters can be probed given an independently inferred total mass profile. The future applications of our method to study cluster cores are promising, given the prospect of collecting more spectro-photometric data of galaxies in cluster lenses (e.g. Yee, Ellingson, & Carlberg 1996a).

With current data, we find strong evidence for the existence of an anisotropic central region. This is consistent

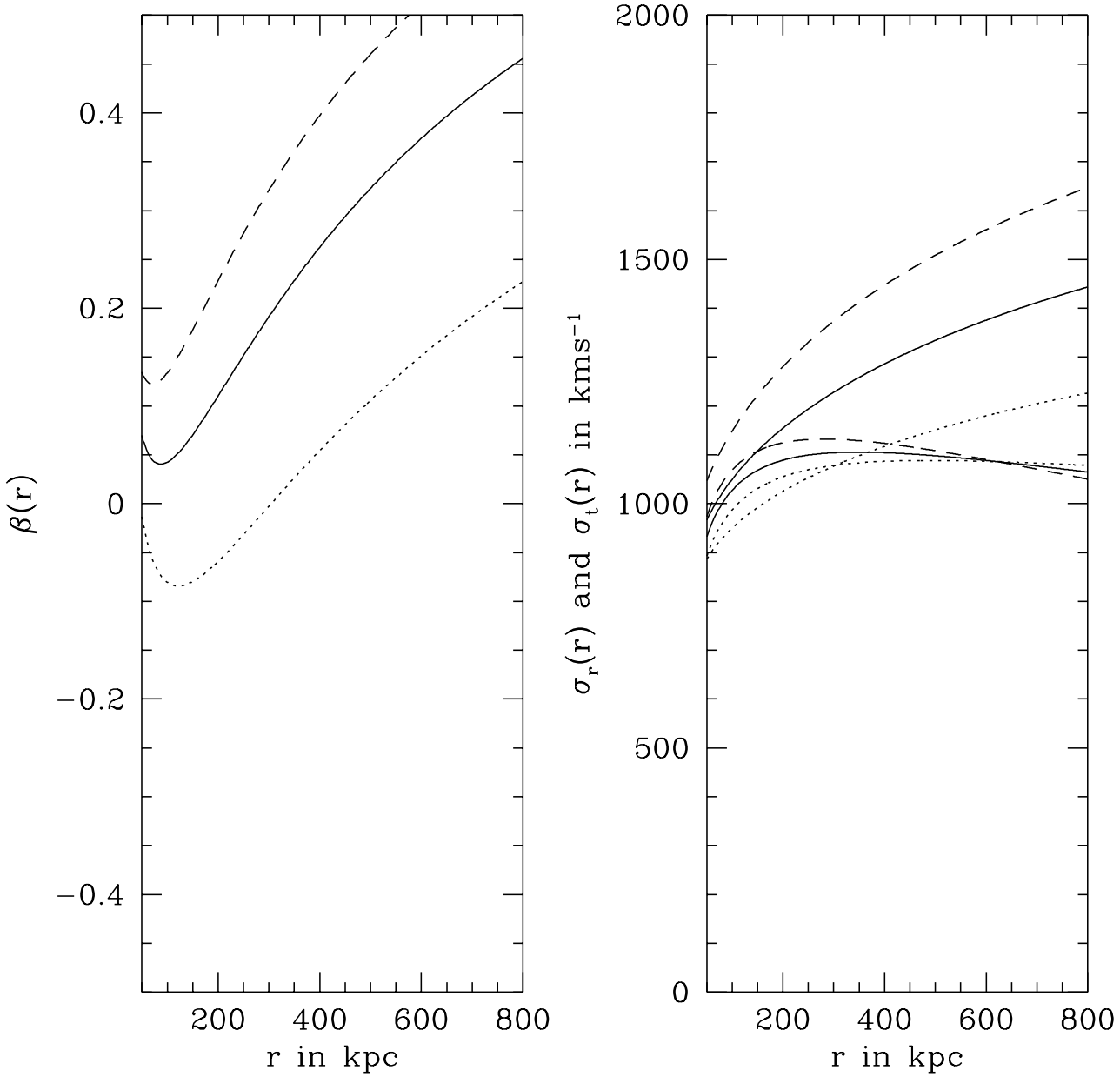

Figure 10. The best fit composite mass model for A2218 : The radial and transverse components of the velocity dispersion and the velocity anisotropy parameter for σ_{los} = 1100, 1200, 1300 km s^{-1} and the galaxy distribution modeled by PROFILE B with $r_s = 200\,h_{50}^{-1}$ kpc and $\alpha = 0.1$.

with the picture of on-going relaxation, wherein anisotropies in the velocity tensor can arise naturally as a consequence of the initial conditions coupled with evolution. Given the range of complex physical processes that operate in cluster cores that could alter galaxy orbits, for instance; dynamical friction (dynamical friction in an aspherical cluster can induce and amplify the velocity anisotropy as demonstrated by Binney (1977), a possible origin for the inferred velocity anisotropy, specially in the case of A2218), potential fluctuations arising due to the presence of substructure and the frequent presence of a cD galaxy at the centre of the cluster potential it is not surprising that the core is not isotropic.

Distinguishing between the dynamical effects of the various physical mechanisms in order to model them satisfactorily, in addition to requiring from the observations more accurately determined line-of-sight velocity dispersion profiles for clusters would enable the application of this technique more effectively. Further extension of this analysis to incorporate the dynamics of the intra-cluster gas with the lensing model self-consistently, is required in order to under-

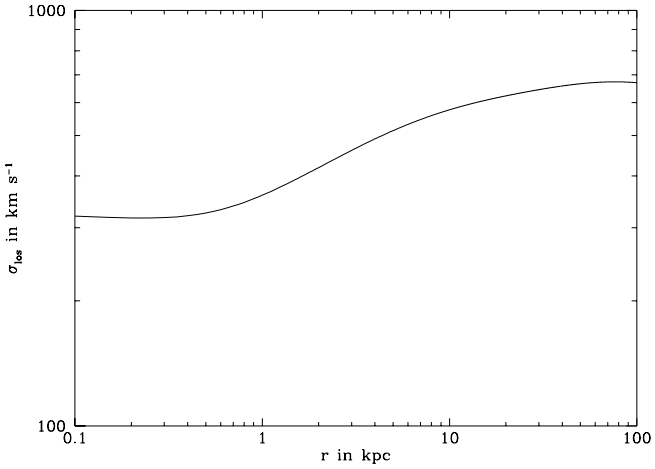

Figure 11. Computed line-of-sight velocity dispersion profile for cD halo stars of A2218

stand the possible role of baryons in the dynamics of cluster cores.

ACKNOWLEDGEMENTS

We thank Martin Rees for his support and encouragement during the course of this work. We acknowledge useful discussions with Richard Ellis, Bernard Fort, Yannick Mellier, Simon White and Tim de Zeeuw. We thank Jens Hjorth and Donald Lynden-Bell for incisive and detailed comments on the draft, Steve Allen for helping with the data processing of the HRI archive data and Roser Pelló for providing us with the A2218 spectro-photometric catalog in computer-readable form. We thank the anonymous referee for useful suggestions. PN acknowledges funding from the Isaac Newton Studentship and Trinity College at the University of Cambridge. JPK acknowledge support from an EC-HCM fellowship.

REFERENCES

Aguilar L., Merritt D., 1990, ApJ, 354, 399
Allen S., Fabian A., Kneib J-P., 1996, MNRAS, 279, 615
Aragon-Salamanca A., Ellis R., Couch W., Carter D., 1993, MNRAS, 262, 764
Bicknell G., Carter D., Killeen N., Bruce T., 1989, ApJ, 336, 639
Binney J., 1977, MNRAS, 181, 735
Binney J., 1982, MNRAS, 200, 951
Blandford R., Kochanek C., 1987, ApJ, 313, 28
Blandford R., Narayan R., 1987, ApJ, 310, 28
Bonnet H., Mellier Y.A&A, 266
Briel U., Henry J., 1995, Nat, 372, 439
Carlberg R., 1994, ApJ, 434, 51
Carlberg R., Yee H. K. C., Ellingson E., Abraham R., Gravel P., Morris S., Pritchet C. J., 1996, ApJ, 462, 32
Cen R., Gnedin N., Ostriker J., 1993, ApJ, 415, 423
Colless M., Dunn A., 1996, ApJ, 458, 435
Crone M., Evrard A., Richstone D., 1994, ApJ, 434, 402
Dressler A., 1979, ApJ, 231, 659
Ebbels T., Kneib J-P., Ellis R., Couch W., Sharples R., 1996, in prep.
Efsthathiou G., Frenk C., Davis M., White S., 1985, ApJS, 57, 241
Evrard A., 1990, ApJ, 363, 349
Fabian A., Hu E., Cowie L., Grindlay J., 1981, ApJ, 248, 47
Fabian A., Nulsen P., Canizares C., 1982, MNRAS, 210, 933
Fahlman G., Kaiser N., Squires G., Woods D., 1994, ApJ, 437, 56
Fisher D., Illingworth G., Franx M., 1995, ApJ, 438, 539
Fort B., Mellier Y., 1994, AARA, 5, 239
Frenk C., Evrard A., White S., Summers F., 1995, astro-ph/9504020, preprint
Gerhard O., 1993, MNRAS, 265, 213
Hjorth J., Madsen J., 1991, MNRAS, 253, 703
Kaiser N., 1995, ApjL, 439, 1
Kaiser N., Squires G., 1993, ApJ, 404, 441
Kaiser N., Squires G., Broadhurst T., 1995, ApJ, 449, 460
Kassiola A., Kovner I., 1993, ApJ, 417, 450
Katgert P., Mazure A., Perea J., den Hartog R., et. al., 1996, A&A, 310, 8
Kent S., Gunn J., 1982, ApJ, 87, 945
Kneib J-P., 1993, in PhD Thesis. Université de Toulouse III
Kneib J-P., Ellis R., Smail I., Couch W., Sharples R.ApJ, 57
Kneib J-P., Mellier Y., Pelló R., Miralda-Escudé J., Le Borgne J., Böhringer H., Picat J., 1995, A&A, 303, 27
Kneib J-P., Soucail G., 1996, in Kochanek C., Hewitt J., eds, Astrophysical Applications of Gravitational Lensing. Kluwer, Dordrecht, p. 113
Le Borgne J., Pelló R., Sanahuja B., 1992, AAPS, 95, 87
Lefevre O., Crampton D., Felenbok P., Monnet G., 1994, A&A, 282, 325
Londrillo P., Messina A., Stiavelli M., 1991, MNRAS, 250, 54
Markevitch M., Mushotzky R., Inoue H., Yamashita K., Furuzawa A., Tawara Y.ApJ, 363
Merritt D., 1987, ApJ, 313, 121
Merritt D., Gebhardt K., 1995, in Durret F., ed, Proc. of the XXIXth Rencontre de Moriond: Clusters of Galaxies. Kluwer, Dordrecht, p. 121
Merritt D., Tremblay B., 1994, AJ, 108, 514
Miralda-Escude J., 1995, ApJ, 438, 514
Natarajan P., Hjorth J., Van Kampen E., 1996, submitted
Navarro J., Frenk C., White S., 1994, MNRAS, 267, 1
Navarro J., Frenk C. S., White S. D. M., 1996, ApJ, 462, 563
Navarro J., White S., 1994, MNRAS, 267, 401
Nulsen P., Böhringer H., 1995, MNRAS, 274, 1093
Pello R., Le Borgne J-F , Sanahuja B., Mathez G., Fort B., 1992, A&A, 266, 6

Sarazin C., 1988, in X-ray emissions from clusters of galaxies. Cambridge Univ. Press, Cambridge
Sharples R., Ellis R., Gray P., 1988, MNRAS, 231, 479
Squires G., Kaiser N., Fahlman G., Woods D., Babul A., 1996, ApJ, 461, 572
The L., White S., 1986, AJ, 92, 1248
Waxman E., Miralda-Escudé J., 1995, ApJ, 451, 451
Yee H., Ellingson E., Carlberg R., 1996a, ApJS (submitted)
Yee H. K. C., Ellingson E., Carlberg R., 1996b, ApjS, 102, 269